Progress In Electromagnetics Research, PIER 82, 1–18, 2008

INVERSE SCATTERING OF AN UN-UNIFORM CONDUCTIVITY SCATTERER BURIED IN A THREE-LAYER STRUCTURE

W. Chien

Electronic Engineering Department
De Lin Institute of Technology
Tu-Cheng, Taipei, R.O.C.

Abstract—We consider the inverse problem of determining both the shape and the conductivity of an un-uniform conductivity scatterer buried in a three-layer structure by the genetic algorithm. An un-uniform conductivity scatterer of unknown shape and conductivity buried in the second layer scatters the incident wave from the first layer or the third layer. We measure the scattered field in the first and third layers. Based on the boundary condition and the measured scattered field, a set of nonlinear integral equations is derived and the imaging problem is reformulated into an optimization problem. The genetic algorithm is then employed to find out the global extreme solution of the object function. As a result, the shape and the conductivity of the scatterer can be obtained. Numerical results are given to demonstrate that even in the presence of noise, good reconstruction has been obtained.

1. INTRODUCTION

The inverse scattering techniques for imaging the shape of imperfectly conducting objects have attracted considerable attention in recent years. They can apply in noninvasive measurement, medical imaging, and biological application. In the past 20 years, many rigorous methods have been developed to solve the exact equation. However, inverse problems of this type are difficult to solve because they are ill-posed and nonlinear. As a result, many inverse problems are reformulated as optimization problems. General speaking, two main kinds of approaches have been developed. The first is based on gradient searching schemes such as the Newton-Kantorovitch method [1–3], the Levenberg-Marguart algorithm [4–6] and the successive-overrelaxation

method [7]. These methods are highly dependent on the initial guess and tend to get trapped in a local extreme. In contrast, the second approach is based on the evolutionary searching schemes [8, 9]. They tend to converge to the global extreme of the problem, no matter what the initial estimate is [10, 11]. Owing to the difficulties in computing the Green's function by numerical method, the problem of inverse scattering in a three-layer structure has seldom been attacked. There are a lot of papers had used the genetic algorithm to solve the problems in many field [12–18], but there are few papers had applied the genetic algorithm to reconstruct the shape of a conductor [19–23]. However, to the best of our knowledge, there are still no numerical results by using the genetic algorithm for an un-uniform conductivity scatterer buried in a three-layer structure. In this paper, we present a computational method to recover the shape of an un-uniform conductivity scatterer buried in a three-layer structure based on the genetic algorithm. The steady state genetic algorithm is used to recover the shape and the conductivity of the scatterer. The steady-state genetic algorithm [24, 25] can reduce the calculation time of the image problem compared with the generational genetic algorithm. In Section 2, the theoretical formulation for the electromagnetic imaging is presented. The general principle of the genetic algorithm and the way we applied them to the imaging problem are described. Numerical results for various objects of different shapes are given in Section 3. Section 4 is the conclusion.

2. THEORETICAL FORMULATION

2.1. Imaging Problem

Let us consider a two-dimensional three-layer structure as shown in Fig. 1, where $(\varepsilon_i, \sigma_i)$ $i = 1, 2, 3$ denote the permittivities and conductivities in each layer and an un-uniform conductivity scatterer is buried in second layer. The metallic cylinder with cross section described by the equation $\rho = F(\theta)$ is illuminated by an incident plane wave whose electric field vector is parallel to the Z axis (i.e., TM polarization). We assume that the time dependence of the field is harmonic with the factor $\exp(j\omega t)$. Let E^{inc} denote the incident field form region 1 with incident angle θ_1 as follow:

$$E^{inc} = E_1^+ e^{+jk_1 \cos\theta_I y} e^{-jk_1 \sin\theta_I x} \hat{z} \tag{1}$$

Owing to the interfaces, the incident plane wave generates three waves that would exist in the absence of the conducting object. Thus, the

unperturbed field is given by

$$E = \begin{cases} E_1 = E_1^+ e^{+jk_1\cos\theta_i y} e^{-jk_1\sin\theta_1 x}\hat{z} + E_1^- e^{-jk_1\cos\theta_1 y} e^{-jk_1\sin\theta_i x}\hat{z} \\ \qquad\qquad\qquad\qquad\qquad\qquad\qquad\qquad\qquad\qquad y \geq a \\ E_2 = E_2^+ e^{+jk_2\cos\theta_2 y} e^{-jk_2\sin\theta_2 x}\hat{z} + E_2^- e^{-jk_2\cos\theta_2 y} e^{-jk_{21}\sin\theta_2 x}\hat{z} \\ \qquad\qquad\qquad\qquad\qquad\qquad\qquad\qquad\qquad\qquad a \geq y \geq -a \\ E_3 = E_3^+ e^{+jk_3\cos\theta_3 y} e^{-jk_3\sin\theta_3 x}\hat{z} \qquad\qquad\qquad\qquad y \leq -a \end{cases} \tag{2}$$

where E_1^+ is set to be 1 and

$$E_1^- = \frac{e^{+j2k_1\cos\theta_1 a}\begin{bmatrix} (Z_1+Z_2)(Z_3-Z_2)e^{-j2k_2\cos\theta_2 a} \\ -(Z_1-Z_2)(Z_3+Z_2)e^{+j2k_2\cos\theta_2 a} \end{bmatrix}}{\begin{bmatrix} (Z_1+Z_2)(Z_3+Z_2)e^{+j2k_2\cos\theta_2 a} \\ -(Z_1-Z_2)(Z_3-Z_2)e^{-j2k_2\cos\theta_2 a} \end{bmatrix}}$$

$$E_2^+ = \frac{1}{2}e^{jk_2(\sin\theta_2 x - \cos\theta_2 a)} \left[\frac{Z_1+Z_2}{Z_1}e^{-jk_1(\sin\theta_1 x - \cos\theta_1 a)} + \frac{Z_1-Z_2}{Z_1}E_1^- e^{-jk_1(\sin\theta_1 x + \cos\theta_1 a)}\right]$$

$$E_2^- = \frac{1}{2}e^{jk_2(\sin\theta_2 x + \cos\theta_2 a)} \left[\frac{Z_1-Z_2}{Z_1}e^{-jk_1(\sin\theta_1 x - \cos\theta_1 a)} + \frac{Z_1+Z_2}{Z_1}E_1^- e^{-jk_1(\sin\theta_1 x + \cos\theta_1 a)}\right]$$

$$E_3^+ = \frac{2Z_3}{Z_2+Z_3}E_2^+ e^{-jk_2(\sin\theta_2 x + \cos\theta_2 a)} e^{jk_3(\sin\theta_3 x + \cos\theta_3 a)}$$

$$k_1\sin\theta_1 = k_2\sin\theta_2 = k_3\sin\theta_3$$
$$k_i^2 = \omega^2\varepsilon_i\mu_0 - j\omega\mu_0\sigma_i \qquad i = 1,2,3 \qquad \mathrm{Im}\,(k_i) \leq 0$$

$$Z_1 = \frac{\eta_1}{\cos\theta_1}, \quad Z_2 = \frac{\varepsilon_2}{\cos\theta_2}, \quad Z_3 = \frac{\eta_3}{\cos\theta_3}$$
$$\eta_1 = \sqrt{\frac{\mu_0}{\varepsilon_1}}, \qquad \eta_2 = \sqrt{\frac{\mu_0}{\varepsilon_2}}, \quad \eta_3 = \sqrt{\frac{\mu_0}{\varepsilon_3}}$$

At an arbitrary point (x, y) (or (r, θ) in polar coordinates) in regions 1 and 3 the scattered field, $\vec{E}_s = \vec{E} - \vec{E}_i$, can be expressed as

$$E_s(\vec{r}) = -\int_0^{2\pi} G(\vec{r}, F(\theta'), \theta')J(\theta')d\theta' \tag{3}$$

where

$$J(\theta) = -j\omega\mu_0\sqrt{F^2(\theta) + F'^2(\theta)}J_s(\theta)$$

and

$$G(x,y;x',y') = \begin{cases} G_1(x,y;x',y'), & y > a \\ G_2(x,y;x',y'), & a > y > -a \\ G_3(x,y;x',y'), & y < -a \end{cases} \tag{4}$$

$$G_1 = \frac{1}{2\pi}\int_{-\infty}^{\infty} je^{-j\gamma_1(y-a)} \frac{(\gamma_2+\gamma_3)e^{j\gamma_2(y'+a)} + (\gamma_2-\gamma_3)e^{-j\gamma_2(y'+a)}}{(\gamma_1+\gamma_2)(\gamma_2+\gamma_3)e^{jr_2(2a)} + (\gamma_1-\gamma_2)(\gamma_2-\gamma_3)e^{-j\gamma_2(2a)}} e^{-j\alpha(x-x')}d\alpha$$

$$G_2 = \frac{1}{2\pi}\int_{-\infty}^{\infty} \frac{j}{2\gamma_2} \left\{ \left[\frac{(\gamma_1+\gamma_2)(\gamma_2+\gamma_3)e^{-j\gamma_2[|y-y'|-2a]} + (\gamma_2-\gamma_1)(\gamma_2-\gamma_3)e^{j\gamma_2[|y-y'|-2a]}}{(\gamma_1+\gamma_2)(\gamma_2+\gamma_3)e^{j\gamma_2(2a)} + (\gamma_1-\gamma_2)(\gamma_2-\gamma_3)e^{-j\gamma_2(2a)}} \right] + \left[\frac{(\gamma_2-\gamma_1)(\gamma_2+\gamma_3)e^{j\gamma_2[y+y']} + (\gamma_2-\gamma_3)(\gamma_1+\gamma_2)e^{-j\gamma_2[y+y']}}{(\gamma_1+\gamma_2)(\gamma_2+\gamma_3)e^{j\gamma_2(2a)} + (\gamma_1-\gamma_2)(\gamma_2-\gamma_3)e^{-j\gamma_2(2a)}} \right] \right\} e^{-j\alpha(x-x')}d\alpha$$

$$G_3 = \frac{1}{2\pi}\int_{-\infty}^{\infty} je^{j\gamma_3(y+a)} \frac{(\gamma_1+\gamma_2)e^{-j\gamma_2(y'-a)} + (\gamma_2-\gamma_1)e^{j\gamma_2(y'-a)}}{(\gamma_1+\gamma_2)(\gamma_2+\gamma_3)e^{jr_2(2a)} + (\gamma_1-\gamma_2)(\gamma_2-\gamma_3)e^{-j\gamma_2(2a)}} e^{-j\alpha(x-x')}d\alpha$$

with

$$\gamma_i^2 = k_i^2 - \alpha^2, \quad i = 1,2,3, \quad \text{and } \mathrm{Im}\,(\gamma_i) \le 0$$

Note that G_1, G_2 and G_3 denote the Green's function which can be obtained by tedious mathematic manipulation for the line source in region 2. Note that we might face some difficulties in calculating the Green's function. The Green's function, given by (4), is in the form of an improper integral which must be evaluated numerically. However, the integral converges very slowly when (x, y) and (x', y') approach the interface. Fortunately, we find that the integral in Green's function may be rewritten as a closed-form term plus a rapidly converging integral (see appendix). Thus the whole integral in the Green's function can be calculated efficiently. $J_s(\theta)$ is the induced surface current density, which is proportional to the normal derivative of the

electric field on the conductor surface. For an un-uniform conductivity scatterer with finite conductivity, the electromagnetic wave is able to penetrate into the interior of a scatterer, so the total tangential electric field at the surface of the scatterer is not equal to zero. As described in [26] and [27], the boundary condition for this case can be approximated by assuming that the total tangential electric field on the scatterer surface is related to surface current density through a surface impedance $Z_s(\omega)$:

$$\hat{n} \times \vec{E} = \hat{n} \times (Z_s \vec{J}_s) \tag{5}$$

where $\hat{n}$ is the outward unit vector normal to the surface of the scatterer. The scatterer of interest here is a nonmagnetic ($\mu = \mu_0$), un-uniform conductivity with minimum radius of curvature a. The surface impedance is expressed in [21] and [22] as $Z_s(\omega, \theta) \cong \sqrt{j\omega\mu_0/\sigma(\theta)}$. This approximation is valid as long as $|\mathrm{Im}\,(N_c)ka| \gg 1$ and $\sigma(\theta) \gg \omega\varepsilon_0$, where "Im" means taking the imaginary part, and N_c is the complex index of refraction of the conductor, given by $N_c = \sqrt{1 + \frac{\sigma(\theta)}{j\omega\varepsilon_0}}$. The boundary condition at the surface of the scatterer given by (5) then yield an integral equation for $J(\theta)$:

$$\vec{E}_2^{inc} + \vec{E}_{2s} = Z_s \vec{J}_s$$

$$E_2^{inc}(\vec{r}) = \int_0^{2\pi} G_2(\vec{r}, F(\theta'), \theta') J(\theta') d\theta' + j\sqrt{\frac{j}{\omega\mu_0\sigma(\theta)}} \frac{J(\theta)}{\sqrt{F^2(\theta) + F'^2(\theta)}} \tag{6}$$

where $\vec{E}_2^{inc}$ is the incident field and $\vec{E}_{2s}$ is the scatter field in second layer.

For the direct scattering problem, the scattered field E_s is calculated by assuming that the shape and conductivity are known. This can be achieved by first solving J in (6) and then calculating E_s using (3). For the inverse problem, assume the approximate center of scatterer, which in fact can be any point inside the scatterer, is known. Then the shape function $F(\theta)$ and conductivity function $\sigma(\theta)$ can be expanded as:

$$F(\theta) = \sum_{n=0}^{N/2} B_n \cos(n\theta) + \sum_{n=1}^{N/2} C_n \sin(n\theta) \tag{7}$$

$$\sigma(\theta) = \sum_{n=0}^{N/2} D_n \cos(n\theta) + \sum_{n=1}^{N/2} E_n \sin(n\theta) \tag{8}$$

where B_n, C_n, D_n and E_n are real coefficient to be determined, and $2\times(N+1)$ is the number of unknowns for shape function and conductivity function. In the inversion procedure, the genetic algorithm is used to minimize the following cost function:

$$CF = \left\{ \frac{1}{M_t} \sum_{m=1}^{M_t} \left| E_s^{\exp}(\vec{r}_m) - E_s^{cal}(\vec{r}_m) \right|^2 / \left| E_s^{\exp}(\vec{r}_m) \right|^2 + \alpha |F'(\theta)|^2 \right\}^{1/2} \tag{9}$$

where M_t is the total number of measurement points. $E_s^{\exp}(\vec{r})$ and $E_s^{cal}(\vec{r})$ are the measured and calculated scattered fields, respectively. The factor $\alpha|F'(\theta)|^2$ can be interpreted as the smoothness requirement for the boundary $F(\theta)$. To make sure that our numerical result (by the moment method) is correct, the scattered field of the cylinder of circular cross section is first calculated by the analytic theorem and compare with those obtained by the moment method, it is found good agreement has been achieved. Moreover, the discretization number for the direct problem is two times that for the inverse problem in our simulation, since it is crucial that the synthetic data generated by a direct solver are not like those obtained by the inverse solver.

2.2. Steady-state Genetic Algorithm

Genetic algorithm is a global numerical optimization method based on genetic recombination and evolution in nature. They use the iterative optimization procedures that start with some randomly selected population of potential solutions, and then gradually evolve toward a better solution through the application of the genetic operators: reproduction, crossover and mutation operators. In our problem, all parameters B_n, C_n, D_n and E_n are encoded using Gray code. We employ steady-state genetic algorithm for the imaging problem investigated. The steady-state genetic algorithm is to insert the new individuals generated by crossover and mutation into the parent population to form a temporary population. We obtained new offspring by using rank selection scheme. As soon as the cost function (CF) changes by $< 1\%$ in two successive generations, the algorithm will be terminated and the final solution is then obtained.

It should be noted that the calculation of the Green's function is quite computational expensive. Steady-state genetic algorithm has not only the characteristic of faster convergence [19, 20], but also the lower rate of crossover. As a result, it is a suitable scheme to effectively save the calculation time for the inverse problem as compared with the generational GA.

3. NUMERICAL RESULTS

We illustrate the performance of the proposed inversion algorithm and its sensitivity to random noise in the scattered field. Consider a lossless three-layer structure ($\sigma_1 = \sigma_2 = \sigma_3 = 0$) and an un-uniform conductivity scatterer buried in region 2. The permittivity in each region is characterized by, $\varepsilon_1 = \varepsilon_0$, $\varepsilon_2 = 2.55\varepsilon_0$ and $\varepsilon_3 = \varepsilon_0$ respectively, as shown in Fig. 1. The frequency of the incident wave is chosen to be 3 GHz, with the incident angles equal to 45° and 315°, respectively. The width of the second layer is 0.3 m. Ten measurement points are equally separated on two parallel lines at equal spacing in region 1 and region 3. Thus there are totally 20 measurements in each simulation. The population size is chosen as 120. The coding length of each unknown coefficient, B_n (C_n, D_n or E_n), is set to be 20 bits. The search range for the unknown coefficient of the shape function is chosen to be from 0 to 0.1 and the unknown coefficient of the conductivity is chosen to be from 1 to 200 S/m. The crossover probability p_c and mutation probability p_m are set to be 0.05 and 0.025. In the following simulation, the CPU time is about six hours per case on P4 3.0 GHz computer.

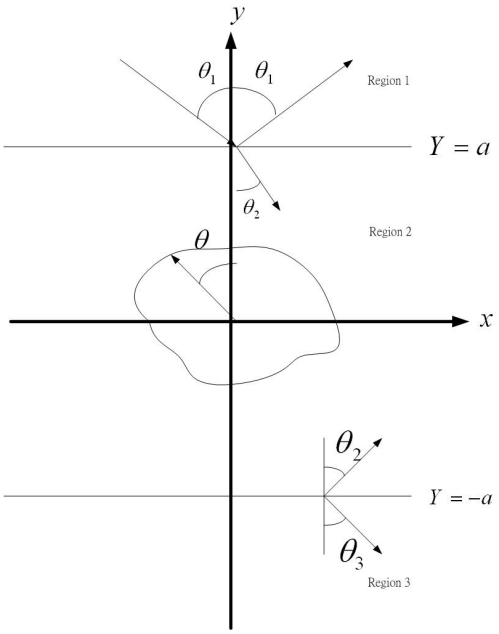

Figure 1. Geometry of the proposed problem in (x, y) plane.

In the first example, the shape and conductivity function are chosen to be $F(\theta) = (0.03 + 0.01 \sin 2\theta)$ m and $\sigma(\theta) = (80 + 20 \cos 2\theta + 20 \sin \theta)$ S/m. The reconstructed shape function and conductivity function for the best population member are plotted in Fig. 2(a) and Fig. 2(b). The errors for the reconstructed shape DR and the reconstructed conductivity DSIG are shown in Fig. 2(c), of which DR

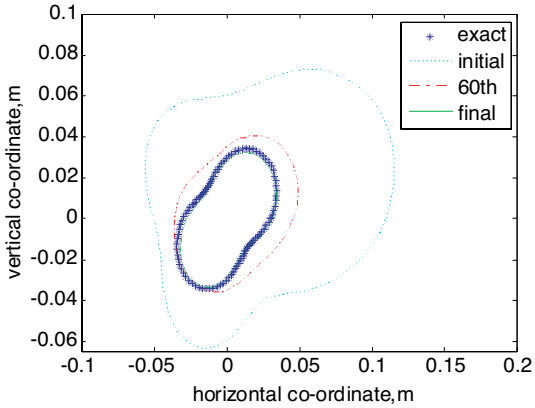

Figure 2a. Shape function for example 1. The star curve represents the exact shape, while the solid curves are calculated shape in iteration process.

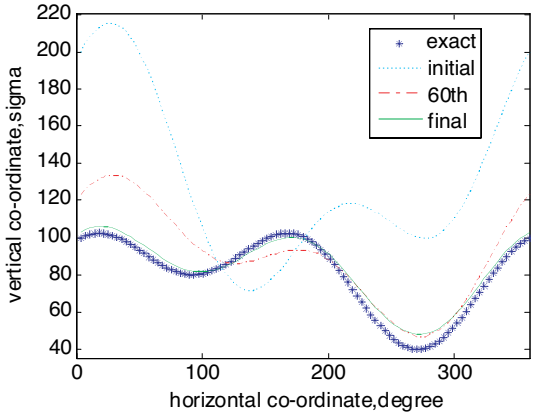

Figure 2b. Conductivity function for example 1. The star curve represents the exact conductivities, while the solid curves are calculated conductivities in iteration process.

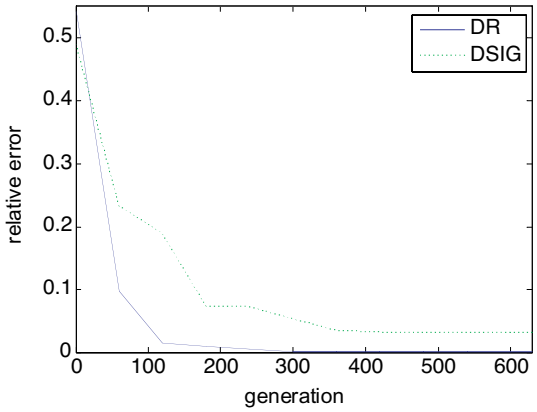

Figure 2c. The shape and conductivity function errors versus generation.

and DSIG are defined as

$$DR = \left\{ \frac{1}{N'} \sum_{i=1}^{N'} \left[F^{cal}(\theta_i) - F(\theta_i) \right]^2 / F^2(\theta_i) \right\}^{1/2} \tag{10}$$

$$DSIG = \left\{ \frac{1}{N'} \sum_{i=1}^{N'} \left[\sigma^{cal}(\theta_i) - \sigma(\theta_i) \right]^2 / \sigma^2(\theta_i) \right\}^{1/2} \tag{11}$$

where N' is set to 100. Quantities DR and $DSIG$ provide measures of how well $F^{cal}(\theta)$ approximates $F(\theta)$ and $\sigma^{cal}(\theta)$ approximates $\sigma(\theta)$, respectively. From Fig. 2a and Fig. 2b, it is clear that the reconstruction of the shape and the conductivity function are quite good. In addition, we also see that the reconstruction of conductivity does not change rapidly toward the exact value until DR is small enough. This can be explained by the fact that the shape function makes a stronger contribution to the scattered field than the conductivity does. In other words, the reconstruction of the shape function has a higher priority than the reconstruction of the conductivity. To investigate the sensitivity of the imaging algorithm against random noise, two independent Gaussian noises with zero mean have been added to the real and imaginary parts of the simulated scattered fields. Normalized standard deviations of $10^{-5}, 10^{-4}, 10^{-3}, 10^{-2}$ and 10^{-1} are used in the simulations. The normalized standard deviation mentioned earlier is defined as the standard deviation of the Gaussian noise divided by the rms value of

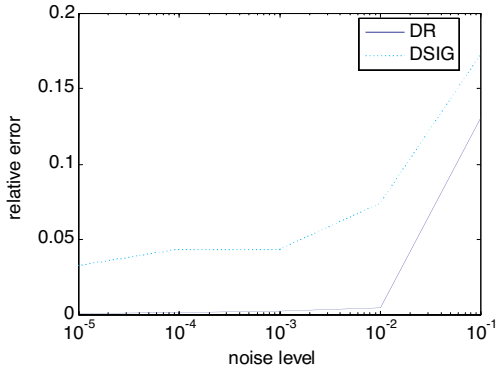

Figure 3. Relative error of shape and conductivity as a function of noise.

the scattered fields. Here, the signal-to-noise ratio (SNR) is inversely proportional to the normalized standard deviation. The numerical result for this example is plotted in Fig. 3. It is understood that the effect of noise is negligible for normalized standard deviations below 10^{-3}.

In the second example, we select the following shape function $F(\theta) = (0.03 + 0.01\cos 3\theta + 0.01\sin\theta)\,\mathrm{m}$ and conductivity function $\sigma(\theta) = (80 + 15\sin\theta + 20\sin 3\theta)\,\mathrm{S/m}$. The purpose of this example is to show that our method is able to reconstruct different shape conductivity. Satisfactory results are shown in Fig. 4a and Fig. 4b.

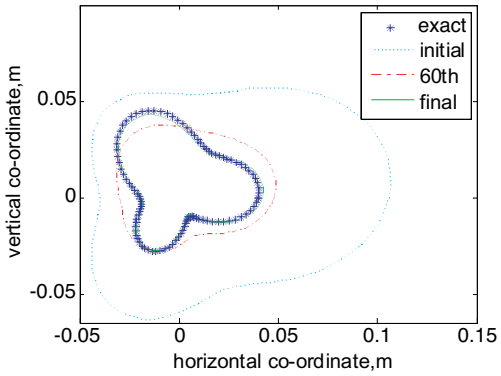

Figure 4a. Shape function for example 2. The star curve represents the exact shape, while the solid curves are calculated shape in iteration process.

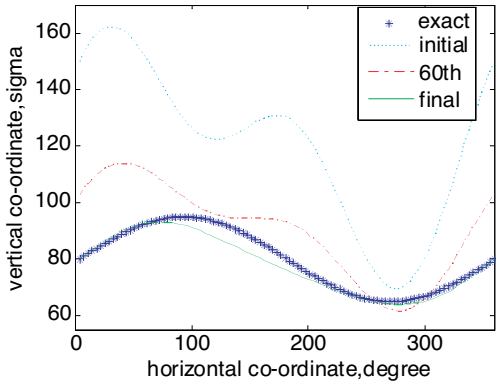

Figure 4b. Conductivity function for example 2. The star curve represents the exact conductivity, while the solid curves are calculated conductivities in iteration process.

In the third example, the shape and conductivity function are selected to be $F(\theta) = (0.05 + 0.02\sin\theta + 0.01\sin 2\theta + 0.02\cos 3\theta)$ m and $\sigma(\theta) = (90 + 15\cos 2\theta + 20\sin\theta + 25\sin 3\theta)$ S/m. Note that the shape function is not symmetrical about either x axis and y axis. This example has further verified the reliability of our algorithm. Refer to Fig. 5a and Fig. 5b for details.

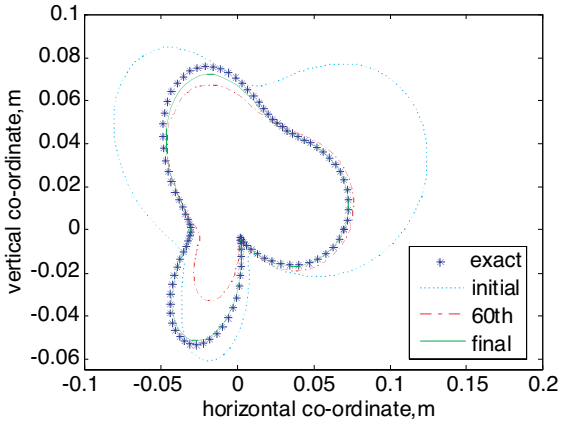

Figure 5a. Shape function for example 3. The star curve represents the exact shape, while the solid curves are calculated shape in iteration process.

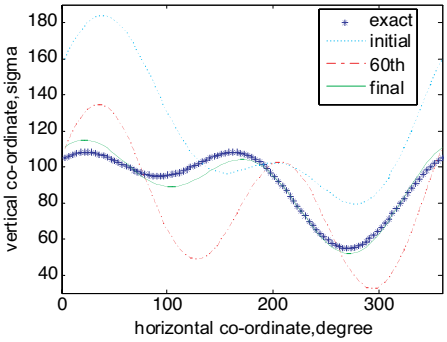

Figure 5b. Conductivity function for example 3. The star curve represents the exact conductivity, while the solid curves are calculated conductivities in iteration process.

4. CONCLUSIONS

We have presented a study of applying the genetic algorithm to reconstruct the shape and the conductivity of an embedded un-uniform conductivity scatterer. Based on the boundary condition and measured scattered field, we have derived a set of nonlinear integral equations and reformulated the imaging problem into an optimization one. The genetic algorithm is then employed to de-embed the microwave image of scatterer. In our experience, the main difficulties in applying the genetic algorithm to the problem are to choose the suitable parameters, such as the population size, coding length of the string (L), crossover probability (p_c), and mutation probability (p_m). Different parameter sets will affect the speed of convergence as well as the computation time. Numerical results illustrate that the conductivity is more sensitive to noise than the shape function is. Numerical results also show that good shape reconstruction can be achieved as long as the normalized noise level is $< 10^{-2}$. But the good conductivity reconstruction can be achieved only the normalized noise level is 10^{-3}.

APPENDIX A.

To calculate the Green's function, we can use the following formula.

$$\int_t^\infty x^{r-1}e^{-\beta x}\cos\delta x dx = \frac{1}{2}(\beta+j\alpha)^{-r}\Gamma[r,(\beta+j\delta)u] + \frac{1}{2}(\beta-j\alpha)^{-r}\Gamma[r,(\beta-j\delta)u] \qquad \text{(A1)}$$

for $\mathrm{Re}\,\beta > |\mathrm{Im}\,\delta|$ where $\Gamma(\alpha, Z) = \int_z^\infty e^{-t}t^{\alpha-1}dt$. Γ is the incomplete Gamma function which has the following properties

$$\Gamma(-n, z) = \frac{(-1)^n}{n!}\left[\Gamma(0, Z) - e^{-z}\sum_{m=0}^{n-1}(-1)^m\frac{m!}{z^{m+1}}\right]$$
$$\Gamma(0, z) = -\gamma - \ln z - \sum_{n=1}^{\infty}(-1)^n\frac{z^n}{(n+1)!} \quad [|\arg(z)| < \pi] \quad \text{(A2)}$$

in which γ is Euler's constant, i.e., $\gamma = 0.5772156649$.

Let us consider the following integral

$$G_1 = \frac{1}{2\pi}\int_{-\infty}^{\infty} je^{-jr_1(y-a)}$$
$$\frac{(r_2+r_3)e^{jr_2(y'+a)} + (r_2-r_3)e^{-jr_2(y'+a)}}{(r_1+r_2)(r_2+r_3)e^{jr_2(2a)} + (r_1-r_2)(r_2-r_3)e^{-jr_2(2a)}}e^{-j\alpha(x-x')}d\alpha$$
$$= \frac{1}{\pi}\int_{-\infty}^{\infty} je^{-jr_1(y-a)}$$
$$\frac{(r_2+r_3)e^{jr_2(y'+a)} + (r_2-r_3)e^{-jr_2(y'+a)}}{(r_1+r_2)(r_2+r_3)e^{jr_2(2a)} + (r_1-r_2)(r_2-r_3)e^{-jr_2(2a)}}\cos\alpha(x-x')d\alpha$$

where $r_i^2 = k_i^2 - \alpha^2,\ i = 1, 2, 3,\ \mathrm{Im}\,(\gamma_i) \le 0,\ y \ge a,\ a \ge y' \ge -a$.

The integral G_1 may be rewritten as follows

$$G_1 = \frac{1}{\pi}\int_0^{\infty} je^{-jr_1(y-a)}$$
$$\frac{(r_2+r_3)e^{jr_2(y'+a)} + (r_2-r_3)e^{-jr_2(y'+a)}}{(r_1+r_2)(r_2+r_3)e^{jr_2(2a)} + (r_1-r_2)(r_2-r_3)e^{-jr_2(2a)}}\cos\alpha(x-x')d\alpha$$
$$+\frac{1}{2\pi}\int_{\alpha_0}^{\infty}\left[\frac{e^{-\alpha(y-y')}}{\alpha} + \frac{\left(k_3^2-k_2^2\right)e^{-\alpha(y+y'+2a)}}{4\alpha^3}\right]\cos\alpha(x-x')d\alpha$$
$$-\frac{1}{2\pi}\int_{\alpha_0}^{\infty}\left[\frac{e^{-\alpha(y-y')}}{\alpha} + \frac{\left(k_3^2-k_2^2\right)e^{-\alpha(y+y'+2a)}}{4\alpha^3}\right]\cos\alpha(x-x')d\alpha$$

in general, we choose $\alpha_0 \gg |k_i|,\ i = 1, 2, 3$.

By Eq. (A1), we get

$$-\frac{1}{2\pi}\int_{\alpha_0}^{\infty}\left[\frac{e^{-\alpha(y-y')}}{\alpha}+\frac{(k_3^2-k_2^2)\,e^{-\alpha(y+y'+2a)}}{4\alpha^3}\right]\cos\alpha(x-x')d\alpha$$

$$=-\frac{1}{4\pi}\{\Gamma[0,[(y-y')+j(x-x')]\alpha_0]+\Gamma[0,[(y-y')-j(x-x')]\alpha_0]\}$$

$$-\frac{(k_3^2-k_2^2)}{16\pi}\left\{\begin{array}{r}[(y+y'+2a)+j(x-x')]^2\\ \Gamma[-2,[(y+y'+2a)+j(x-x')]\alpha_0]\\ +[(y+y'+2a)-j(x-x')]^2\\ \Gamma[-2,[(y+y'+2a)-j(x-x')]\alpha_0]\end{array}\right\}$$

Using the above relation, we obtain

$$G_1=\frac{1}{\pi}\int_{-\infty}^{\infty}je^{-jr_1(y-a)}$$

$$\frac{(r_2+r_3)e^{jr_2(y'+a)}+(r_2-r_3)e^{-jr_2(y'+a)}}{(r_1+r_2)(r_2+r_3)e^{jr_2(2a)}+(r_1-r_2)(r_2-r_3)e^{-jr_2(2a)}}\cos\alpha(x-x')d\alpha$$

$$-\frac{1}{2\pi}\int_{\alpha_0}^{\infty}\left[\frac{e^{-\alpha(y-y')}}{\alpha}+\frac{(k_3^2-k_2^2)\,e^{-\alpha(y+y'+2a)}}{4\alpha^3}\right]\cos\alpha(x-x')d\alpha$$

$$-\frac{1}{4\pi}\{\Gamma[0,[(y-y')+j(x-x')]\alpha_0]+\Gamma[0,[(y-y')-j(x-x')]\alpha_0]\}$$

$$-\frac{(k_3^2-k_2^2)}{16\pi}\left\{\begin{array}{r}[(y+y'+2a)+j(x-x')]^2\\ \Gamma[-2,[(y+y'+2a)+j(x-x')]\alpha_0]\\ +[(y+y'+2a)-j(x-x')]^2\\ \Gamma[-2,[(y+y'+2a)-j(x-x')]\alpha_0]\end{array}\right\} \tag{A3}$$

Now, the integral G_1 is written as a rapidly converging integral plus a dominate integral. We can use Eq. (A3) to evaluate G_1 by means of Simpson's rule easily. Similarly,

$$G_2=\frac{1}{\pi}\int_{-\infty}^{\infty}\frac{j}{2r_2}$$

$$\left\{\left[\frac{(r_1+r_2)(r_2+r_3)e^{-jr_2[|y-y'|-2a]}+(r_2-r_1)(r_2-r_3)e^{jr_2[|y-y'|-2a]}}{(r_1+r_2)(r_2+r_3)e^{jr_2(2a)}+(r_1-r_2)(r_2-r_3)e^{-jr_2(2a)}}\right]\right.$$

$$\left.\left[\frac{(r_2-r_1)(r_2+r_3)e^{jr_2[y+y']}+(r_2-r_3)(r_1+r_2)e^{-jr_2[y+y']}}{(r_1+r_2)(r_2+r_3)e^{jr_2(2a)}+(r_1-r_2)(r_2-r_3)e^{-jr_2(2a)}}\right]-\frac{je^{-jr_2|y-y'|}}{2r_2}\right\}$$

$$\cos\alpha(x-x')d\alpha + \frac{j}{4}H_0^{(2)}\left(k_2\sqrt{(x-x')+(y-y')}\right)$$

$$+\frac{1}{2\pi}\int_{\alpha_0}^{\infty}\left[\begin{array}{l}\dfrac{\left(k_3^2-k_2^2\right)\left(k_1^2-k_2^2\right)e^{-\alpha[4a-|y-y'|]}}{16\alpha^5}+\\ \dfrac{\left(k_1^2-k_2^2\right)}{4}\dfrac{e^{-\alpha(2a-y-y')}}{\alpha^3}+\dfrac{\left(k_3^2-k_2^2\right)}{4}\dfrac{e^{-\alpha(y'+y+2a)}}{\alpha^3}\end{array}\right]\cos\alpha(x-x')d\alpha$$

$$-\frac{\left(k_1^2-k_2^2\right)}{16\pi}\left\{\begin{array}{r}[(2a-y-y')+j(x-x')]^2\\ \Gamma[-2,[(2a-y-y')+j(x-x')]\alpha_0]\\ +[(2a-y-y')-j(x-x')]^2\\ \Gamma[-2,[(2a-y-y')-j(x-x')]\alpha_0]\end{array}\right\}$$

$$-\frac{\left(k_3^2-k_2^2\right)}{16\pi}\left\{\begin{array}{r}[(y+y'+2a)+j(x-x')]^2\\ \Gamma[-2,[(y+y'+2a)+j(x-x')]\alpha_0]\\ +[(y+y'+2a)-j(x-x')]^2\\ \Gamma[-2,[(y+y'+2a)-j(x-x')]\alpha_0]\end{array}\right\}$$

$$-\frac{\left(k_1^2-k_2^2\right)\left(k_3^2-k_2^2\right)}{64\pi}\left\{\begin{array}{r}[4a-|y-y'|+j(x-x')]^4\\ \Gamma[-4,[4a-|y-y'|+j(x-x')]\alpha_0]\\ +[4a-|y-y'|-j(x-x')]^4\\ \Gamma[-4,[4a-|y-y'|-j(x-x')]\alpha_0]\end{array}\right\}$$

And

$$G_3 = \frac{1}{2\pi}\int_{-\infty}^{\infty} je^{jr_3(y+a)}$$

$$\frac{(r_1+r_2)e^{-jr_2(y'-a)}+(r_2-r_1)e^{jr_2(y'-a)}}{(r_1+r_2)(r_2+r_3)e^{jr_2(2a)}+(r_1-r_2)(r_2-r_3)e^{-jr_2(2a)}}e^{-j\alpha(x-x')}d\alpha$$

$$= \frac{1}{\pi}\int_{-\infty}^{\infty} je^{jr_3(y+a)}$$

$$\frac{(r_1+r_2)e^{-jr_2(y'-a)}+(r_2-r_1)e^{jr_2(y'-a)}}{(r_1+r_2)(r_2+r_3)e^{jr_2(2a)}+(r_1-r_2)(r_2-r_3)e^{-jr_2(2a)}}e^{-j\alpha(x-x')}d\alpha$$

$$+\frac{1}{2\pi}\int_{\alpha_0}^{\infty}\left[\frac{e^{-\alpha(y-y')}}{\alpha}+\frac{\left(k_1^2-k_2^2\right)e^{-\alpha(2a-y-y')}}{4\alpha^3}\right]\cos\alpha(x-x')d\alpha$$

$$-\frac{1}{4\pi}\left\{\Gamma[0,[(y'-y)+j(x-x')]\alpha_0]\Gamma[0,[(y'-y)-j(x-x')]\alpha_0]\right\}$$

$$-\frac{(k_1^2-k_2^2)}{16\pi}\left\{\begin{array}{r}[(2a-y-y')+j(x-x')]^2\\ \Gamma[-2,[(2a-y-y')+j(x-x')]\alpha_0]\\ +[(2a-y-y')-j(x-x')]^2\\ \Gamma[-2,[(2a-y-y')-j(x-x')]\alpha_0]\end{array}\right\} \tag{A4}$$

REFERENCES

1. Roger, A., "Newton-Kantorovitch algorithm applied to an electromagnetic inverse problem," *IEEE Trans. Antennas Propagat.*, Vol. AP-29, 232–238, Mar. 1981.
2. Tobocman, W., "Inverse acoustic wave scattering in two dimensions from impenetrable targets," *Inverse Problems*, Vol. 5, 1131–1144, Dec. 1989.
3. Chiu, C. C. and Y. W. Kiang, "Electromagnetic imaging for an imperfectly conducting cylinders," *IEEE Trans. Microwave Theory Tech.*, Vol. 39, 1632–1639, Sept. 1991.
4. Colton, D. and P. Monk, "A novel method for solving the inverse scattering problem for time-harmonic acoustic waves in the resonance region II," *SIAM J. Appl. Math.*, Vol. 46, 506–523, June 1986.
5. Kirsch, A., R. Kress, P. Monk, and A. Zinn, "Two methods for solving the inverse acoustic scattering problem," *Inverse Problems*, Vol. 4, 749–770, Aug. 1988.
6. Hettlich, F., "Two methods for solving an inverse conductive scattering problem," *Inverse Problems*, Vol. 10, 375–385, 1994.
7. Kleiman, R. E. and P. M. van den Berg, "Two-dimensional location and shape reconstruction," *Radio Sci.*, Vol. 29, 1157–1169, July/Aug. 1994.
8. Xiao, F. and H. Yabe, "Microwave imaging of perfectly conducting cylinders from real data by micro genetic algorithm coupled with deterministic method," *IEICE Trans. Electron.*, Vol. E81-C, No. 12, 1784–1792, Dec. 1998.
9. Chiu, C. C. and W. T. Chen, "Electromagnetic imaging for an imperfectly conducting cylinder by the genetic algorithm," *IEEE Trans. Microwave Theory and Tec.*, Vol. 48, 1901–1905, Nov. 2000.
10. Goldgerg, D. E., *Genetic Algorithm in Search, Optimization and Machine Learning*, Addison-Wesley, 1989.
11. Rahmat-Samiia, Y. and E. Michielessen, *Electromagnetic Optimization by Genetic Algorithms*, Wiley Interscience, 1999.

12. Tu, T. C. and C. C. Chiu, "Path loss reduction in an urban area by genetic algorithms," *J. of Electromagn. Waves and Appl.*, Vol. 20, No. 3, 319–330, 2006.
13. Tian, Y. B. and J. Qian, "Ultraconveniently finding multiple solutions of complex transcendental equations based on genetic algorithm," *J. of Electromagn. Waves and Appl.*, Vol. 20, No. 4, 475–488, 2006.
14. Lu, Y. Q. and J. Y. Li, "Optimization of broad band top-load antenna using micro-genetic algorithm," *J. of Electromagn. Waves and Appl.*, Vol. 20, No. 6, 793–801, 2006.
15. Chen, X., D. Liang, and K. Huang, "Microwave imaging 3-D buried objects using parallel genetic algorithm combined with FDTD technique," *J. of Electromagn. Waves and Appl.*, Vol. 20, No. 13, 1761–1774, 2006.
16. Mitilineos, S. A., S. C. Thomopoulos, and C. Capsalis, "Genetic design of dual-band, switched-beam dipole arrays, with elements failure conrrection, retaining constant excitation coefficients," *J. of Electromagn. Waves and Appl.*, Vol. 20, No. 14, 1925–1942, 2006.
17. Ayestaran, R. G., J. Laviada-Martinez, and F. Las-Heras, "Synthesis of passive-dipole array with a genetic-neural hybrid method," *J. of Electromagn. Waves and Appl.*, Vol. 20, No. 15, 2123–2135, 2006.
18. Zhai, Y.-W., X.-W. Shi, and Y.-J. Zhao, "Optimized design of ideal and actual transformer based on improved micro-genetic algorithm," *J. of Electromagn. Waves and Appl.*, Vol. 21, No. 13, 1761–1771, 2006.
19. Chiu, C. C. and P. T. Liu, "Image reconstruction of a perfectly conducting cylinder by the genetic algorithm," *IEE Proc. Microw. Antennas Propag.*, Vol. 143, 249–253, June 1996.
20. Xiao, F. and H. Yabe, "Microwave imaging of perfectly conducting cylinders from real data by micro genetic algorithm couple with deterministic method," *IEICE Trans. Electron.*, Vol. E81-C, Dec. 1998.
21. Meng, Z. Q., T. Takenaka, and T. Tanaka, "Image reconstruction of two-dimensional impenetrable objects using genetic algorithm," *Journal of Electromagnetic Waves and Applications*, Vol. 13, 95–118, 1999.
22. Qian, Z. P., Z. Y. Ding, and W. Hong, "Application of genetic algorithm and boundary element method to electromagnetic imaging of two-dimensional conducting targets," *5th International Symposium on ISAPE*, 211–214, 2000.

23. Li, C. L., S. H. Chen, C. M. Yang, and C. C. Chiu, "Image reconstruction for a patially immersed perfectly conducting cylinder using the steady state algorithm," *Radio Sci.*, Vol. 39, RS2016, April 2004.
24. Vavak, F. and T. C. Fogarty, "Comparison of steady state and generational genetic algorithms for use in nonstationary environments," *Proceedings of IEEE International Conference on Evolutionary Computation*, 192–195, 1996.
25. Johnson, J. M. and Y. Rahmat-Samii, "Genetic algorithms in engineering electromagnetics," *IEEE Trans. Antennas Propagat.*, Vol. 39, 7–21, Aug. 1997
26. Tesche, F. M., "On the inclusion of loss in time domain solutions of electromagnetic interaction problems," *IEEE Trans. Electromagn. Compat.*, Vol. 32, 1–4, 1990.
27. Jordan, E. C. and K. G. Balmain, *Electromagnetic Waves and Radiating Systems*, Prentice-Hall, Englewood Cliffs, NJ, 1968.